Transport suppression by shear flow generation in multihelicity resistive-g turbulence

H. Sugama

National Institute for Fusion Science, Nagoya 464-01, Japan

W. Horton

Institute for Fusion Studies, The University of Texas at Austin, Austin, Texas 78712

Turbulent momentum transport given by the Reynolds stress is considered as a candidate for explaining the production and sustainment of the mean shear flow in the high confinement "(H)" mode. The fluctuation mechanism for the shear flow generation and transport reduction in the three-dimensional (3-D) multihelicity system is given. The profiles of the Reynolds stress, shear flow, and thermal flux in the 3-D case are compared with those in the two-dimensional (2-D) case. The Beklemishev–Horton theory for the anomalous transport which multiplies the 2-D transport by the density of distinct mode rational surfaces is found to overestimate the observed flux due to the disappearance of a subset of modes on certain rational surfaces. The mixing-length theory, in which the anomalous transport is independent of the density of mode rational surfaces, underestimates the thermal flux.

I. INTRODUCTION

In this work we are concerned with the problem of the interaction of multiple helicity modes as influenced by the mean shear flow generated through the resistive-g plasma turbulence.[1,2] The rate of generation of the flow and the influence of the mean shear flow in single-helicity resistive-g modes is investigated in Carreras et al.[3] and Sugama and Horton.[4] In those works it is demonstrated that the radial divergence of the turbulent flux of poloidal momentum $\rho\langle \tilde{v}_x \tilde{v}_y \rangle$, where ρ is the mass density, can produce a sharp transition to a lower level of turbulence with an appreciably lower thermal flux. In this single-helicity case a tangent hyperbolic-like mean $\mathbf{E}_r \times \mathbf{B}$ flow profile is generated about the mode rational surface. The question arises as to how well this simple picture survives in the case of nearby coupled mode rational surfaces. Here we report that the description of the shear suppression changes as a function of the density of mode rational surfaces.

A theoretical description of two limiting results for the transport as a function of the density of the mode rational surfaces is given by Beklemishev and Horton.[5] We show here that the actual outcome for the dependence of the thermal flux $q = \langle \tilde{v}_x \tilde{p} \rangle$ on the density of mode rational surfaces is bounded between the two theoretical idealizations for reasons that lie outside the scope of the idealized descriptions.

The first standard model[6] is that the thermal flux is independent of the density of mode rational surfaces. The model assumes that as the number of modes in each radial interval increases, their amplitudes decrease such that there is an equipartition of the fixed total fluctuation energy to each mode. This may be called the equipartition model and is essentially the mixing-length model since that model does not depend on the density of states.

The second alternative model, advanced by Beklemishev and Horton,[5] is that the modes *do not* equipartition the available fluctuation energy. This part of the Beklemishev–Horton model (hereafter called the BH model) model is borne out by the simulations presented here.

The second assertion of the BH model is that each (distinct) mode localized on its corresponding rational surface reaches roughly the same amplitude obtained in the single-helicity limit. The total thermal flux is thus approximately the density of distinct mode rational surfaces times the single-helicity flux. The idea of the BH model can be supported if the single-helicity nonlinear self-interactions are much stronger than the interactions between modes with different helicities.

From the simulations reported here we see that this Beklemishev–Horton model is defeated (at least for the resistive-g turbulence considered here) by the fact that the nonlinear interactions between modes on neighboring rational surfaces are strong. In fact, in one case the interaction eliminates every other localized mode. In this case the computed flux is approximately one-half the BH value but still more than twice the equipartition value. These mode-interaction effects directly relate to the effectiveness of the generation of the mean shear flow since this flow generation process is also localized to the mode rational surfaces and would be reduced substantially in the standard models with the equipartitioning of energy on each rational surface.

The work is organized as follows: In Sec. II we introduce the standard nonlinear partial differential equations for resistive-g turbulence and review the relation between the dimensional and dimensionless equations and variables. In Sec. III we present the simulation results for the single helicity and multiple helicity simulations. In the multiple helicity problem three different densities of the mode rational surfaces are compared with each other and the single-helicity results. In Sec. IV the conclusions and observations are given.

II. MODEL EQUATIONS

In order to describe the resistive-g turbulence, we use the following equations[2,4] for the electrostatic potential

$\phi \equiv \phi_0 + \tilde{\phi}$ and the pressure $p \equiv P_0 + \tilde{p}$ (the subscript 0 denotes the background part and the fluctuation part)

$$\frac{\rho_m c}{B_0}\left(\frac{\partial}{\partial t} - \mu \nabla_\perp^2 + \frac{c}{B_0}\hat{z}\times\nabla\phi\cdot\nabla\right)\nabla_\perp^2\phi$$

$$= -\frac{B_0}{c\eta}\nabla_\parallel^2\phi - \Omega'\,\frac{\partial\tilde{p}}{\partial y}, \tag{1}$$

$$\left(\frac{\partial}{\partial t} - \chi\nabla_\perp^2 + \frac{c}{B_0}\hat{z}\times\nabla\phi\cdot\nabla\right)\tilde{p} = \frac{c}{B_0}P_0'\frac{\partial\phi}{\partial y}, \tag{2}$$

where B_0 is the component of the static magnetic field along the z axis, ρ_m the average mass density, c the light velocity in the vacuum, η the resistivity, μ the viscosity, χ the pressure diffusivity, $P_0' \equiv dP_0/dx$ (<0) the background pressure gradient, and $\Omega' \equiv d\Omega/dx$ (>0) the average curvature of the magnetic field line,[2] $\nabla_\perp^2 = \partial_x^2 + \partial_y^2$ denotes the two-dimensional Laplacian. The gradient along the static sheared magnetic field line is given by

$$\nabla_\parallel = \frac{\partial}{\partial z} + \frac{x}{L_s}\frac{\partial}{\partial y}. \tag{3}$$

Here $B_0, L_s, \rho_m, \eta, \chi, P_0'$, and Ω' are assumed to be constant since we treat a local transport problem. The electrostatic approximation is used in Eqs. (1) and (2) since we consider the low-beta plasma in the peripheral region.

The dissipation coefficients μ and χ are included to give an energy sink in the high wave number region, which is necessary for the turbulence saturation. We consider that they are dominated by the ion–ion collision and given by the classical or neoclassical expressions.

Hereafter we use the resistive-g units given by

$$[t] = (-P_0'\Omega'/\rho_m)^{-1/2} = \sqrt{L_p L_c}/v_T,$$

$$[x] = [y] = cL_s\eta^{1/2}(-\rho_m P_0'\Omega')^{1/4}/B_0$$

$$\qquad = L_s(\nu_e v_T/\omega_{ce}\omega_{ci}\sqrt{L_p L_c})^{1/2},$$

$$[z] = L_s,$$

$$[\mu] = [\chi] = c[\phi]/B_0 = [x]^2/[t] = c^2\eta(-P_0')\Omega' L_s^2/B_0^2$$

$$\qquad = D_{cl}(L_s^2/L_p L_c),$$

$$[p] = P_0'[x], \tag{4}$$

where $\nu_e = n_e e^2\eta/m_e$ is the electron collision frequency, $D_{cl} = c^2\eta P_0/B_0^2$ the classical diffusivity, $\omega_{ce} = eB_0/m_e c$, $\omega_{ci} = eB_0/m_i c$ the cyclotron frequencies, $v_T = \sqrt{(T_i + T_e)/m_i}$, $L_c = 1/\Omega'$, and $L_p = -P_0/P_0'$. Then we obtain model equations in nondimensional variables from Eqs. (1) and (2) as follows:

$$\partial_t\nabla_\perp^2\phi + [\phi,\nabla_\perp^2\phi] = -\nabla_\parallel^2\phi - \partial_y\tilde{p} + \mu\nabla_\perp^4\phi, \tag{5}$$

$$\partial_t\tilde{p} + [\phi,\tilde{p}] = -\partial_y\phi + \chi\nabla_\perp^2\tilde{p}, \tag{6}$$

where

$$\nabla_\parallel = \partial_z + x\partial_y, \quad [f,g] = (\partial_x f)(\partial_y g) - (\partial_x g)(\partial_y f). \tag{7}$$

The equation for the background poloidal flow $v_E \equiv d\phi_0/dx$ is derived from Eq. (5) as

$$\partial_t v_E = -\partial_x\langle\tilde{v}_x\tilde{v}_y\rangle + \mu\partial_x^2 v_E. \tag{8}$$

Here $-\langle\tilde{v}_x\tilde{v}_y\rangle \equiv \langle(\partial_x\tilde{\phi})(\partial_y\tilde{\phi})\rangle$ represents the Reynolds stress caused by the potential fluctuations and $\langle\ \cdot\ \rangle \equiv (L_y L_z)^{-1}\int_0^{L_y} dy \int_0^{L_z} dz$ is the average on the (y,z) surface with the periodic lengths L_y and L_z. Equation (8) follows from averaging Eq. (5) over y and z, integrating once in x, and using $v_E(x,t) = \partial\phi(x,t)/\partial x$, where ϕ is $y-z$ average of $\phi(x,y,t)$. The Reynolds stress term in Eq. (8) is derived from the average of the nonlinear term in Eq. (5) as

$$\langle[\tilde{\phi},\nabla_\perp^2\tilde{\phi}]\rangle = \langle\nabla_\perp\cdot[\tilde{\phi},\nabla_\perp\tilde{\phi}]\rangle$$

$$= \partial_x\langle[\tilde{\phi},\partial_x\tilde{\phi}]\rangle$$

$$= \partial_x\langle\partial_y\{(\partial_x\tilde{\phi})(\partial_x\tilde{\phi})\} - \partial_x\{(\partial_y\tilde{\phi})(\partial_x\tilde{\phi})\}\rangle$$

$$= -\partial_x^2\langle(\partial_y\tilde{\phi})(\partial_x\tilde{\phi})\rangle.$$

In deriving Eq. (8) from Eq. (5), an integration in x is performed and we put the constant of integration as zero.

III. SIMULATION RESULTS

Equations (5) and (6) are numerically solved in the sheared slab configuration. Hereafter, we consider the hydrogen plasma in the peripheral region with the parameters given by

$$B = 1 \text{ T}, \quad T_e = T_i = 50 \text{ eV}, \quad n_e = 1\times10^{19} \text{ m}^{-3},$$

$$L_s = 1 \text{ m}, \quad L_s^2/L_p L_c = 10. \tag{9}$$

In this case, Eq. (4) gives

$$[t] = 3.2\times10^{-6} \text{ s}, \quad [x] = 1.3\times10^{-4} \text{ m},$$

$$[z] = 1 \text{ m}, \quad [\mu] = [\chi] = [x]^2/[t] = 5.0\times10^{-3} \text{ m}^2/\text{s}. \tag{10}$$

Then using the Braginskii ion classical viscosity and thermal diffusivity, the normalized dissipation coefficients in Eqs. (5), (6), and (8) are given by

$$\mu = 0.46\left(\frac{m_i}{m_e}\right)^{1/2}\frac{(T_e/T_i)^{1/2}}{1+T_i/T_e}\frac{L_p L_c}{L_s^2} \approx 1.0, \tag{11}$$

$$\chi = 2.0\left(\frac{m_i}{m_e}\right)^{1/2}\frac{(T_i/T_e)^{1/2}}{(1+T_i/T_e)^2}\frac{L_p L_c}{L_s^2} \approx 2.2. \tag{12}$$

It should be noted that the normalized dissipation coefficients are independent of the magnitudes of the magnetic field, density, and temperatures and determined by the geometrical factor $L_s^2/L_p L_c$ and the ratio between the ion and electron temperatures.

The potential and pressure fluctuations are Fourier expanded as

$$\begin{pmatrix}\tilde{\phi}\\\tilde{p}\end{pmatrix} = \sum_{mn}\begin{bmatrix}\phi_{mn}(x)\\p_{mn}(x)\end{bmatrix}\exp\left[2\pi i\left(\frac{my}{L_y}+\frac{nz}{L_z}\right)\right], \tag{13}$$

where L_y and L_z denote the maximum poloidal and toroidal wavelength. Since the value of the minimum poloidal wavelength L_y/M (M: the maximum poloidal mode number) are determined by requiring that the dissipation coefficients μ,χ yield a strong short wavelength damping, the maximum po-

loidal wavelength L_y used in the simulations is limited by the maximum number of modes admitted by the computer memory. A typical value employed here is $L_y/2\pi=20$, which corresponds to a poloidal wavelength of 1.6 cm, i.e., 22 times larger than the ion thermal Larmor radius for the plasma parameters in Eq. (9).

We put the boundaries at $x=\pm a$, which are chosen such that the fluctuations are damped enough by the magnetic shear before reaching them. We employ the boundary conditions given by

$$\tilde{\phi}=\partial_x^2\tilde{\phi}=\tilde{p}=0 \quad (\text{at } x=\pm a). \qquad (14)$$

Since we are concerned with the background shear flow production due to the Reynolds stress, we neglect the quasilinear pressure flattening implied by the $y-z$ average of Eq. (6), that is, take $\langle p_{00}=0\rangle$. This fixing of the background pressure gradient to the value of $1/L_p$ which appears as unity in the coefficient of the $\partial_y\phi$ term in Eq. (6) is a standard simulation procedure. The procedure of fixing the background pressure gradient is equivalent to the addition of a source heating term to the pressure equation that is such as to exactly cancel the $y-z$ average of the $[\phi,p]$ term. This heating term is written as $q=\langle[\tilde{\phi},\tilde{p}]\rangle=\partial_x\langle\tilde{p}\tilde{v}_x\rangle$. For reference, see Ref. 7.

Figures 1(a) and 1(b) show the linear growth rates for the resistive-g mode under the background poloidal in the form of $v_E(x)=V_0 \sin(\pi x/2a)$. Here $a=30$ is used, which is much larger than the mode width. The maximum vorticity (or shear) is given by $V_0' = \pi V_0/2a$. The dependence of the growth rates on the poloidal wave number $k_y\equiv 2\pi m/L_y$ is shown for $V_0' = 0, 0.3, 0.6$ in Fig. 1(a) and that on V_0' for the minimum wave number $k_y=0.05$. We can see that the system is completely linearly stable for $V_0' \geqslant 0.56$. It should be noted that, due to the radial symmetry of the system, the stability and the growth rates are independent of the sign of V_0'.

A. Single-helicity simulations

Here the results of the single-helicity nonlinear simulation are described for comparison with those of the multihelicity case as shown later. The shear flow generation in this case was already reported in our previous paper. There it was shown that the vortex tilting in the resistive-g mode under the small shear flow gives the Reynolds stress which produces the large shear flow and the resultant turbulence suppression. It was also shown that the shear flow generation by the Reynolds stress is more effective when the viscous damping of the background flow is weaker.

In Eq. (13), $L_y=20\times2\pi$ and $a=30$ is used for the maximum poloidal wavelength and the modes with $|m|\leqslant12$ and $n=0$ are included. Here $|m|\leqslant6$ corresponds to the linearly unstable modes. In this case, we obtain the multiple saturated states which depend on the initial conditions. This dependence is similar to the results of Carreras et al.[3] In the saturated states, a certain linearly unstable mode dominates all other modes and its poloidal mode number characterizes the saturated state. It is found in the simulations that the smaller the dominant poloidal mode number is, the larger the saturation level becomes, even if the linear growth rates are decreased for lower mode numbers. Figure 2 shows the time
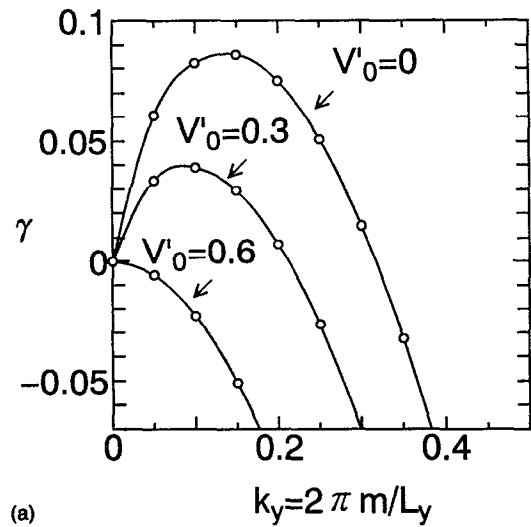
(a)
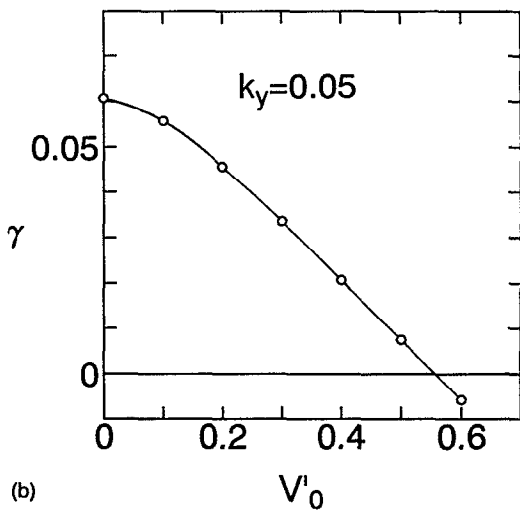
(b)

FIG. 1. The linear growth rates for the resistive-g mode under the background poloidal flow. (a) Dependence on the poloidal wave number k_y for different values of the vorticity (or shear) V_0': $V_0' = 0$ (no background flow case), 0.3 and 0.6. (b) Dependence on V_0' in the case of $k_y=0.05$.

evolution of the kinetic energy and the turbulent transport in the case where the mode with the lowest poloidal mode number, i.e., $m=1$ is dominant.

Here it should be remarked that, for more strongly turbulent states, the energy tends to concentrate on the lowest number mode through the inverse energy cascade process. As an example, Fig. 3 shows the time evolution of the kinetic energy in the case where $L_y=100/3\times2\pi$ is used. In this case, both the total mode number and the linearly unstable mode number are 5/3 times larger than in the case of Fig. 2, and the more turbulent behavior is realized. In Fig. 3, perturbations with the same kinetic energy and a random phase relation are initially given to all the single-helicity modes and the background flow is fixed as $v_E=0$. Then, the most unstable mode ($m=5$) grows into the dominant mode in the first saturated state although we finally have the saturation with the $m=1$ mode dominant. Thus as far as no additional damping term for lower wave numbers is assumed in the model equations (5) and (6), the $m=1$ mode (or the largest poloidal wave-
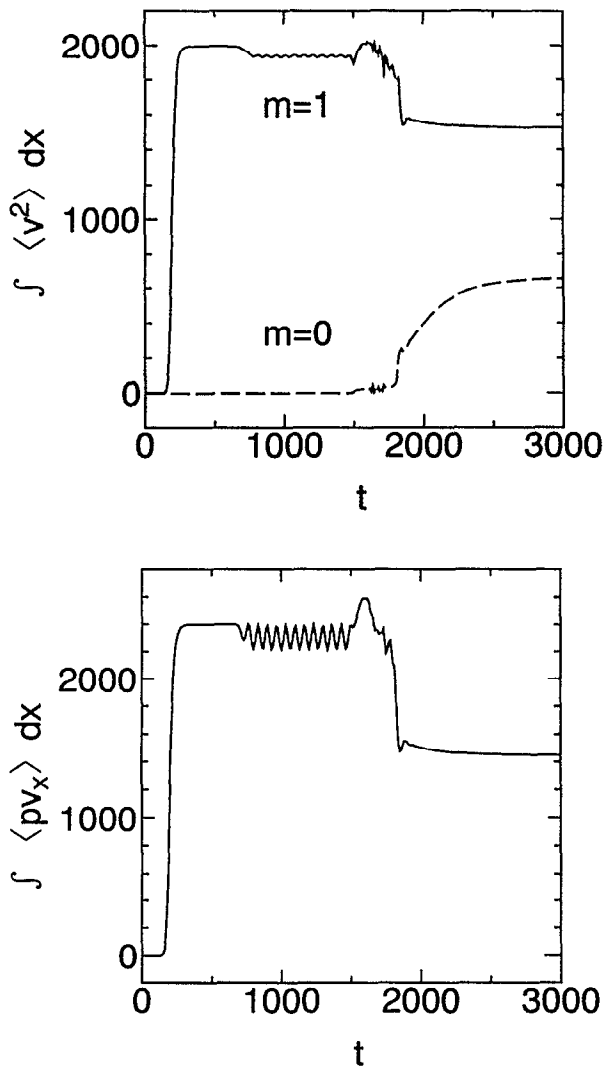
H. Sugama and W. Horton

FIG. 2. The time evolution of the kinetic energy $\frac{1}{2}\int\langle v^2\rangle dx$ (top) and the convective transport $\int\langle\bar{p}\bar{v}_x\rangle dx$ (bottom) in the single-helicity case with $L_y/2\pi=20$. Here the $m=1$ mode is dominant in the saturated state. The background flow v_E is fixed as $v_E=0$ for $0<t<1000$ and v_E is given by solving Eq. (8) for $t>1000$. The background flow kinetic energy ($m=0$) as well as the dominant mode ($m=1$) kinetic energy is plotted.

length mode) dominates the final saturated state in the strongly turbulent system using the larger values for L_y.

We consider the $m=1$ mode dominant case shown in Fig. 2 as a standard single-helicity result for $L_y/2\pi=20$ for comparison with the multihelicity cases. In Fig. 2, the background flow is fixed as $v_E=0$ for $0<t<1000$ in order to obtain the L-mode type saturation while v_E is given by solving Eq. (8) for $t>1000$. At $t\sim1800$ with some delay after the change of the simulation conditions we see the low "(L)" to high "(H)" L–H confinement mode transition, i.e., the generation of the background shear flow ($m=0$) and the reduction of the fluctuation and transport. Figure 4 shows radial profiles of the convective profile $\langle\bar{p}\bar{v}_x\rangle$ at the L mode (a solid line, $t=1000$) and the H mode (a dashed line, $t=3000$) phases in the case of Fig. 2. The turbulent transport is reduced to a factor of 2/3 by the L–H transition. If we estimate the anomalous thermal diffusivity by $\chi_{th}=\frac{3}{2}\langle\bar{p}\bar{v}_x\rangle_{max}/(-P_0')$ and express it dimensionally, we obtain from Fig. 4
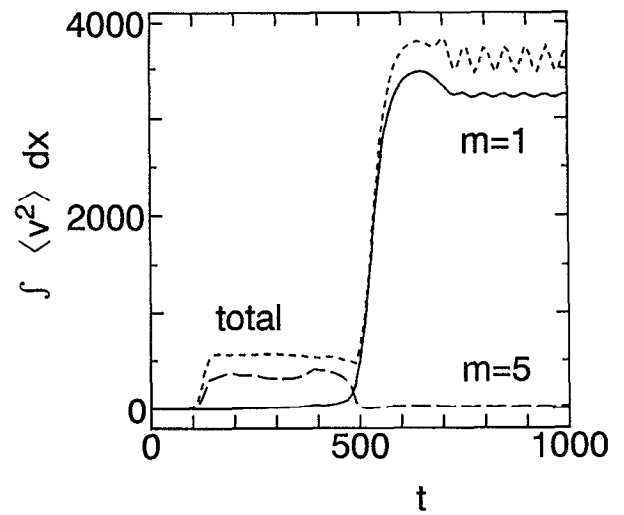

FIG. 3. The time evolution of the kinetic energy $\frac{1}{2}\int\langle v^2\rangle dx$ in the single-helicity case with $L_y/2\pi=100/3$. Here initial perturbations with the same kinetic energy and a random phase relation are given to all the single-helicity modes and the background flow is fixed as $v_E=0$ all the time.

$\chi_{th}\simeq1.5$ m^2/s for the L mode and $\chi_{th}\simeq1.0$ m^2/s for the H mode. Radial profiles of the background shear flow and the Reynolds stress $\langle\bar{v}_x\bar{v}_y\rangle$ in the H-mode phase ($t=3000$) are shown in Figs. 5(a) and 5(b), respectively. The flow profile is an odd function of x similar to the hyperbolic tangent. The maximum value of the shear or the vorticity is $v_E'(x=0)=0.62$, which is larger than the critical value for the linear stability 0.56. Since the signs of $v_E'(x)$ and $\langle\bar{v}_x\bar{v}_y\rangle$ are the same, the energy transfer is from the fluctuation to the background flow, at the rate given by $\langle\bar{v}_x\bar{v}_y\rangle v_E'>0$. Thus in the H mode, the fluctuation level is lowered through the Reynolds stress transferring the fluctuation energy to the background mean shear flow kinetic energy. That is, the fluctuations transport the ρv_E momentum up the v_E gradient in
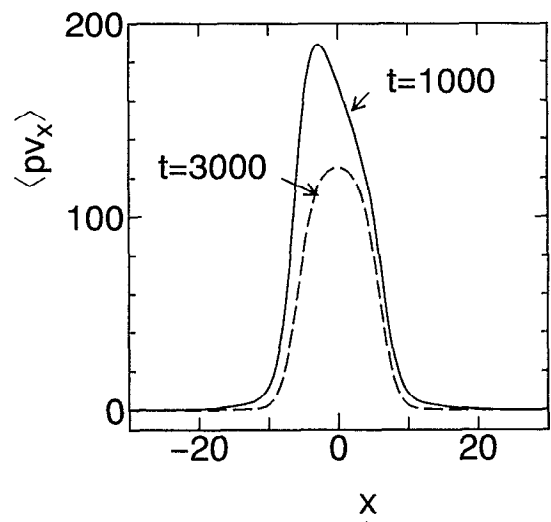

FIG. 4. Radial profiles of the convective flux $\langle\bar{p}\bar{v}_x\rangle$ for $t=1000$ (a solid line) and $t=3000$ (a dashed line) in the case of Fig. 2.
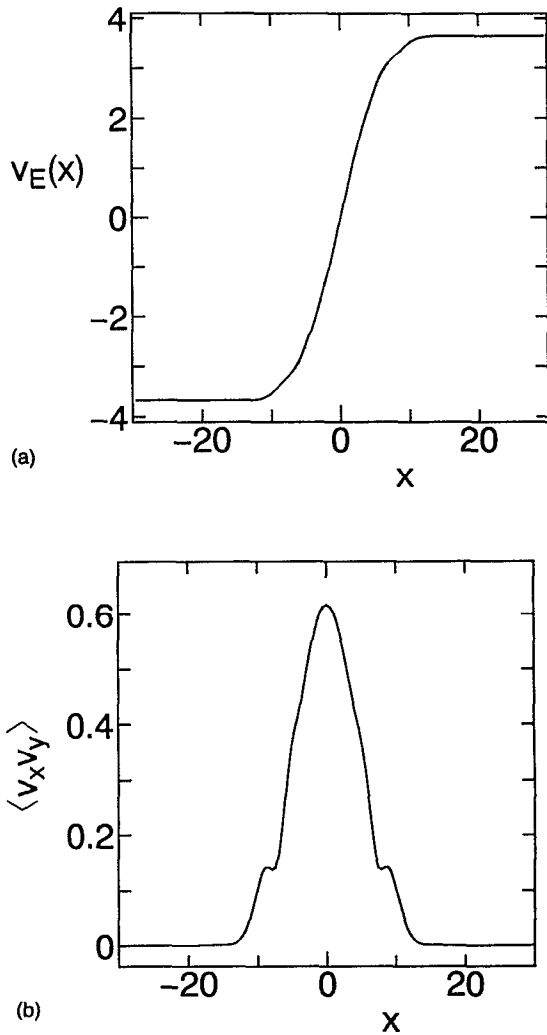
FIG. 5. Radial profiles of (a) the background poloidal flow $v_E(x)$ and (b) the Reynolds stress $\langle \tilde{v}_x \tilde{v}_y \rangle$ at the time $t=3000$ in the case of Fig. 2.

B. Multihelicity simulations

In the multihelicity simulations we use the same values for μ, χ, and L_y as in the single-helicity case shown in Fig. 2. In all the multihelicity simulations, we include the modes with $|m| \leqslant 11$ and $|n| \leqslant 2m$. Thus the number of modes with the largest poloidal wavelength, i.e., the $m=1$ modes, is five ($n=0,\pm1,\pm2$). Initially, perturbations with the same kinetic energy and the random phase relation are given only to the $m=1$ modes in order to obtain the saturated state with the $m=1$ modes dominant, compared to the single-helicity result in Fig. 2. Another important parameter in the multihelicity cases is the maximum toroidal wavelength L_z in Eq. (13). The positions of the rational mode surfaces are represented by $x=-(L_y/L_z)(n/m)$ and therefore the interval between the $m=1$ modes is given by $\Delta \equiv L_y/L_z$. [Here it should be noted that the magnetic shear length L_s is unity in our units (4). The density of states for a general $q(r)=rB_z/RB_\theta$ profile from Eq. (6) of Ref. 5 is $\rho_m(r)=m6|q'|/\pi^2 q^2$ where $6/\pi^2 \simeq 0.608$ is the fraction of irreducible mode rational surfaces with given $m=k_y r$ mode number. Locally this density is $1/\Delta$ for $m=1$ in the present simulations with constant L_s.] From Fig. 4, the radial width W of the $m=1$ mode is roughly given by $W=20$. In order to examine the dependence of the transport on Δ, we use three different values for L_z, i.e., $L_z/2\pi=1,4/3,8/3$ which correspond to $\Delta=20,15,7.5$, respectively. It is expected that the overlap or direct interaction between the adjacent $m=1$ modes is weak for $\Delta=20$, moderate for $\Delta=15$ and much strong for $\Delta=7.5$.

Figure 6 shows the time evolution of $\int dx \langle \tilde{v}^2 \rangle$ and $\int dx \langle \tilde{p}\tilde{v}_x \rangle$ in the multihelicity cases of $\Delta=20,15,7.5$. Here the background flow is fixed as $v_E=0$ and we also plot the kinetic energy and transport in the case of Fig. 2 multiplied by five for comparison. We can see that the turbulence level in the multihelicity case is lower than predicted from simple superposition of the independent single-helicity subsystems which is given by the dashed line at $5\times200=10\,000$. The turbulent transport per active, single $m=1$ mode remains about the same ($\sim150-200$ for the three active modes) but the multihelicity interactions suppress two of the five modes. Figure 7 shows radial profiles of the convective flux $\langle \tilde{p}\tilde{v}_x \rangle$ for the three multihelicity cases in Fig. 6 at the saturated states. For $\Delta=7.5$, the profiles of the two modes with $m=1$ and $n=\pm1$ almost disappear in contrast with the dominant contributions from the modes with $m=1$ and $n=0,\pm2$. In the multihelicity cases, we find that the large vortices with low poloidal mode numbers suppress their neighboring modes. Then, we can find only one peak within the width W of the $m=1$ modes, i.e., when the $m=1$ modes exist inside the interval W, only one of them survives. The reason that the total turbulent kinetic energy and transport decreases for smaller Δ is this annihilation or damping of some $m=1$ modes *rather than* a homogeneous decrease of each $m=1$ mode energy. Thus when the interactions between modes with different helicities is large, the total transport is not simply proportional to the radial distribution density of the unstable modes, since they reduce the number of the modes with significant contributions to transport. The total transport is also not given by the model of equipartition in which all m modes share the same total fixed energy level (with that level given
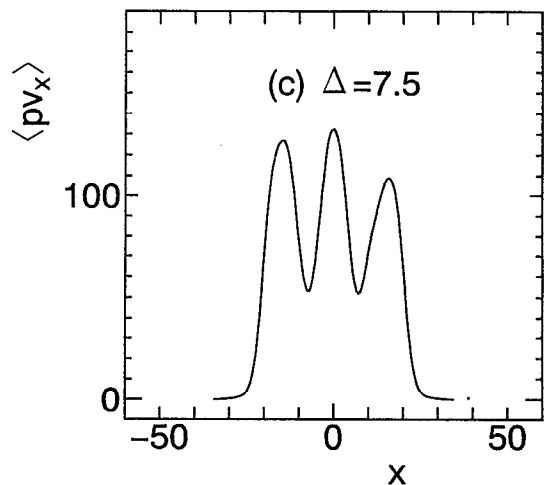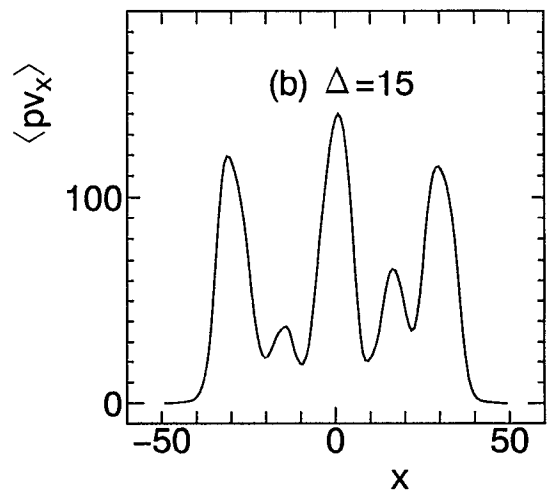
contrast to collisional viscosity which always transport the momentum down the gradient $[\langle v_x v_y \rangle^{\text{coll}} v_E' = -\mu(dv_E/dx)^2 < 0$, where μ is the positive definite collisional viscosity].

The linear resistive-g modes in the absence of any shear flow have a symmetry in the radial structure such that a single, isolated mode cannot produce a radially asymmetric shear flows. However, we find in Figs. 2, 4, and 5 that the transition from the initial radially symmetric state with no flow to the final asymmetric state with the shear flow, which is a typical example of a spontaneously broken symmetry. The asymmetry in the radial mode structure is caused by the nonlinear interaction between the modes with different phases. The property of the radial symmetry in the resistive-g modes is reflected by the fact that both signs of the flow shear are realized with the same probability. In our previous work[4] we showed that the key parameter for the L–H transition is the shear flow damping coefficient and that the transition to high-shear flow-low transport occurs when the damping coefficient is smaller than some critical value.
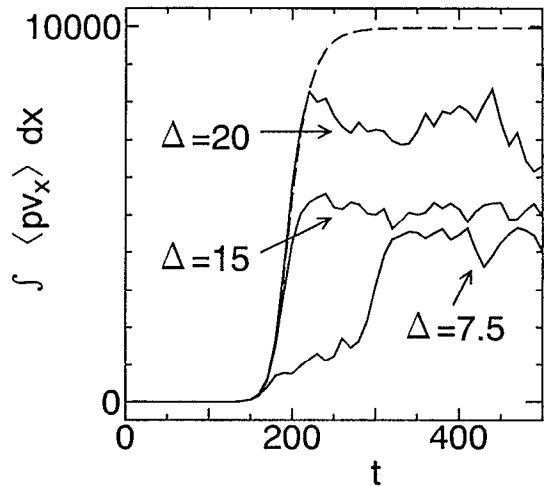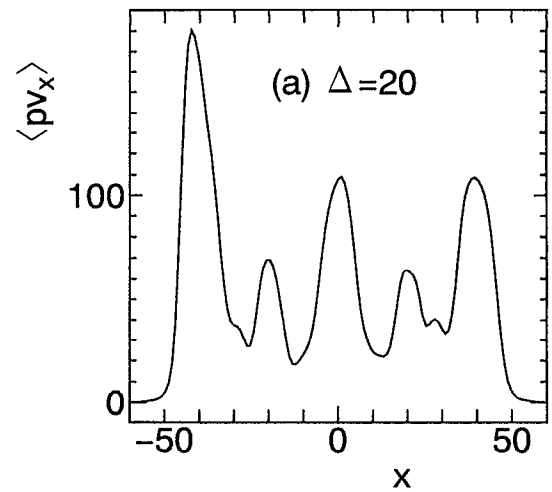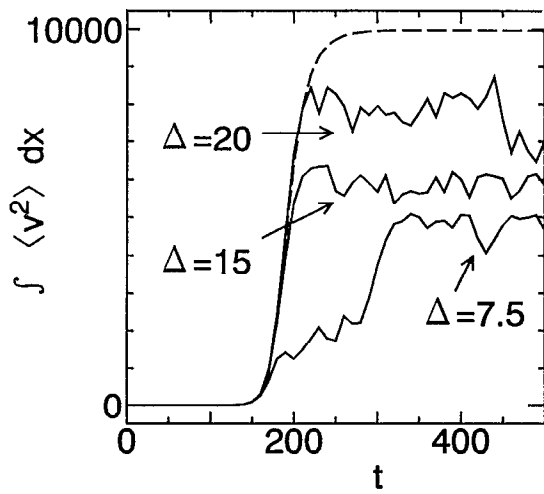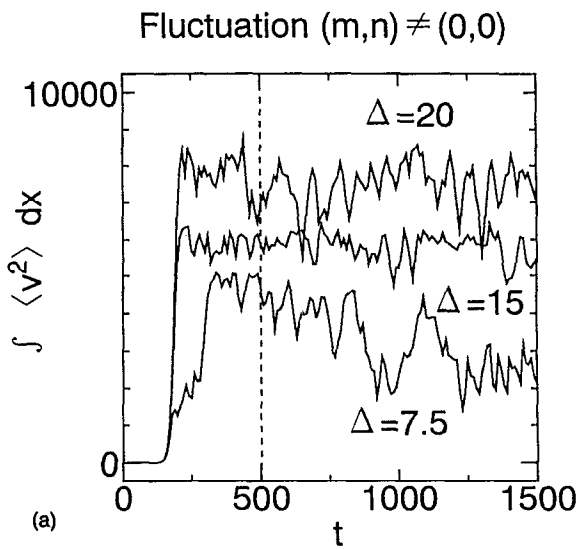
H. Sugama and W. Horton

FIG. 6. The time evolution of the kinetic energy $\frac{1}{2}\int\langle v^2\rangle dx$ (top) and the convective transport $\int\langle\bar{p}\bar{v}_x\rangle dx$ (bottom) in the multihelicity cases with $L_y/2\pi=20$ for different values of the interval between the adjacent $m=1$ modes Δ: $\Delta=20$, 15, and 7.5. Here the modes with $|m|\leqslant 11$ and $|n|\leqslant 2m$ are included and perturbations with the same kinetic energy and the random phase relation are initially given only to the $m=1$ modes ($n=0$, ±1 ±2). The background flow v_E is fixed as $v_E=0$. Dashed lines represent the kinetic energy and transport in the single-helicity case of Fig. 2 multiplied by 5.
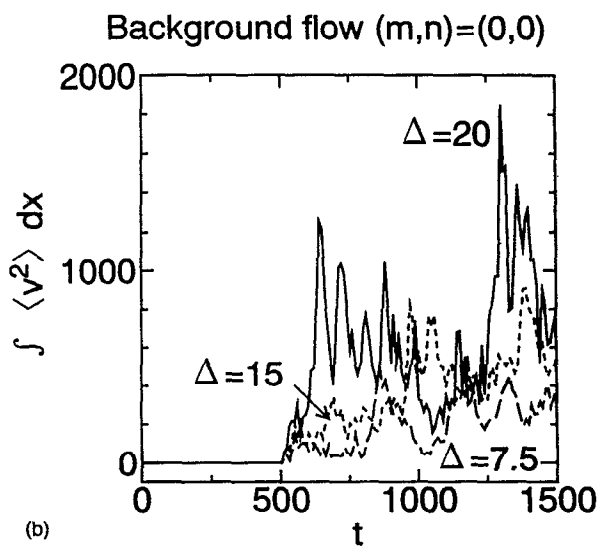
by the mixing-length formula for example). The situation as described here is a more complex one with the total transport level lying between these two extreme limiting models. The two limits are analyzed in Beklemishev and Horton,[5] but the disappearance of some of the primary modes was not taken into account in the BH model. In the absence of shear flow generation the computed flux is approximately one-half the BH value and *three times* the single helicity value.

Next, in order to investigate the shear flow generation by the Reynolds stress, we continue the simulations in Fig. 2 with the temporal evolution of the background flow $v_E(x,t)$ included by solving Eq. (8). Figure 8 shows the time evolution of the turbulent kinetic energy and transport, where the same results in Fig. 2 are plotted for $0\leqslant t\leqslant 500$ and v_E is allowed to evolve for $t>500$. The time evolution of the background flow kinetic energy is also shown in Fig. 8 for the three cases of $\Delta=20,15,7.5$. It is seen that the reduction of

FIG. 7. Radial profiles of the convective flux $\langle\bar{p}\bar{v}_x\rangle$ in the three cases of Fig. 6 for $t=500$: (a) $\Delta=20$, (b) $\Delta=15$, and (c) $\Delta=7.5$.
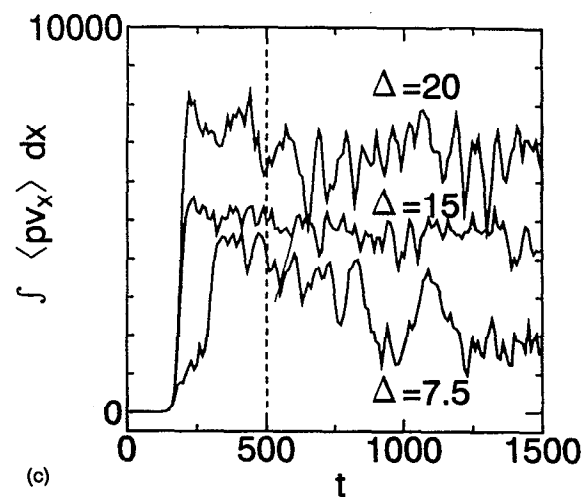
the turbulent kinetic energy and transport accompanied by the background flow generation at $t>500$ is the most clear for $\Delta=7.5$ and not so for $\Delta=15,20$. Radial profiles of $\langle\bar{p}\bar{v}_x\rangle$, v_E, $\langle\bar{v}_x\bar{v}_y\rangle$ and $\langle\bar{v}_x\bar{v}_y\rangle v_E'$ in the cases of Fig. 8 are given in

Fluctuation (m,n) ≠ (0,0)

$\int \langle v^2 \rangle\, dx$

Δ=20

Δ=15

Δ=7.5

10000

0

0   500   1000   1500

t

(a)

Background flow (m,n)=(0,0)

$\int \langle v^2 \rangle\, dx$

2000

1000

0

Δ=20

Δ=15

Δ=7.5

0   500   1000   1500

t

(b)

$\int \langle pv_x \rangle\, dx$

10000

Δ=20

Δ=15

Δ=7.5

0

0   500   1000   1500

t

(c)

FIG. 8. The time evolution of (a) the turbulent kinetic energy, (b) the background flow kinetic energy, and (c) the convective transport in the multihelicity case with $L_y/2\pi=20$ for $\Delta=20$, 15, and 7.5. Here the same $v_E=0$ case results as in Fig. 6 are given for $0<t<500$. For $t>500$, v_E is given by solving Eq. (8).

$\langle pv_x \rangle$

(a) Δ=20

100

0

−50   0   50

x

$\langle pv_x \rangle$

(b) Δ=15

100

0

−50   0   50

x

$\langle pv_x \rangle$

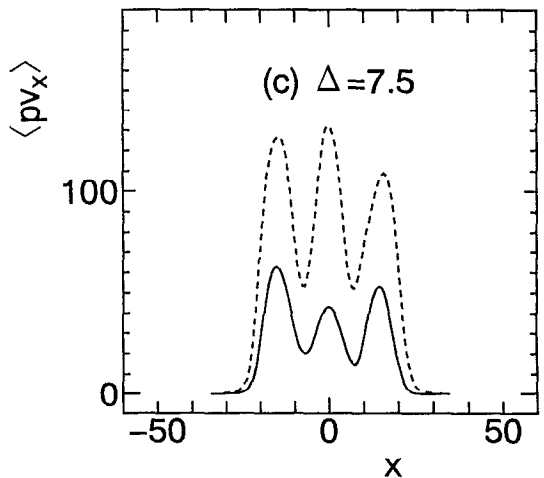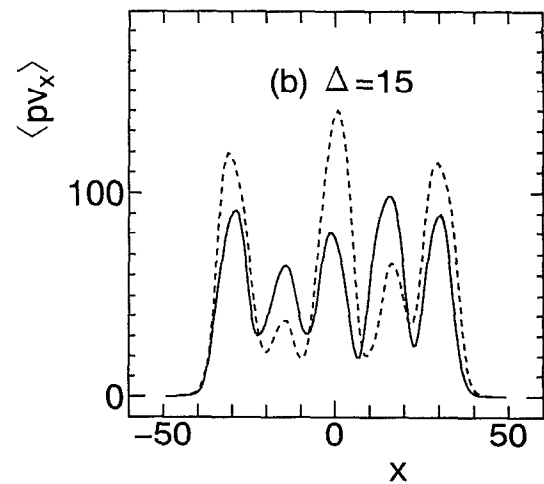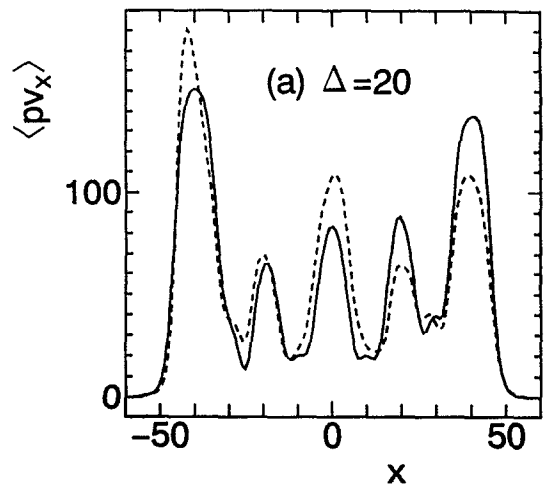(c) Δ=7.5

100

0

−50   0   50

x

FIG. 9. Radial profiles of the convective flux $\langle \tilde{p}\tilde{v}_x \rangle$ in the three cases of Fig. 8 for $t=500$ (dotted lines) and $t=1500$ (solid lines): (a) $\Delta=20$, (b) $\Delta=15$, and (c) $\Delta=7.5$.

Figs. 9 and 10. The dashed line in Fig. 9 gives the thermal flux $\langle \tilde{v}_x \tilde{p} \rangle$ calculated at $t=500$ where $v_E=0$.

As seen from Fig. 9, the peak values of $\langle \tilde{p}\tilde{v}_x \rangle$ at $t=1500$ (solid lines) tend to decrease for smaller Δ. Interestingly, in
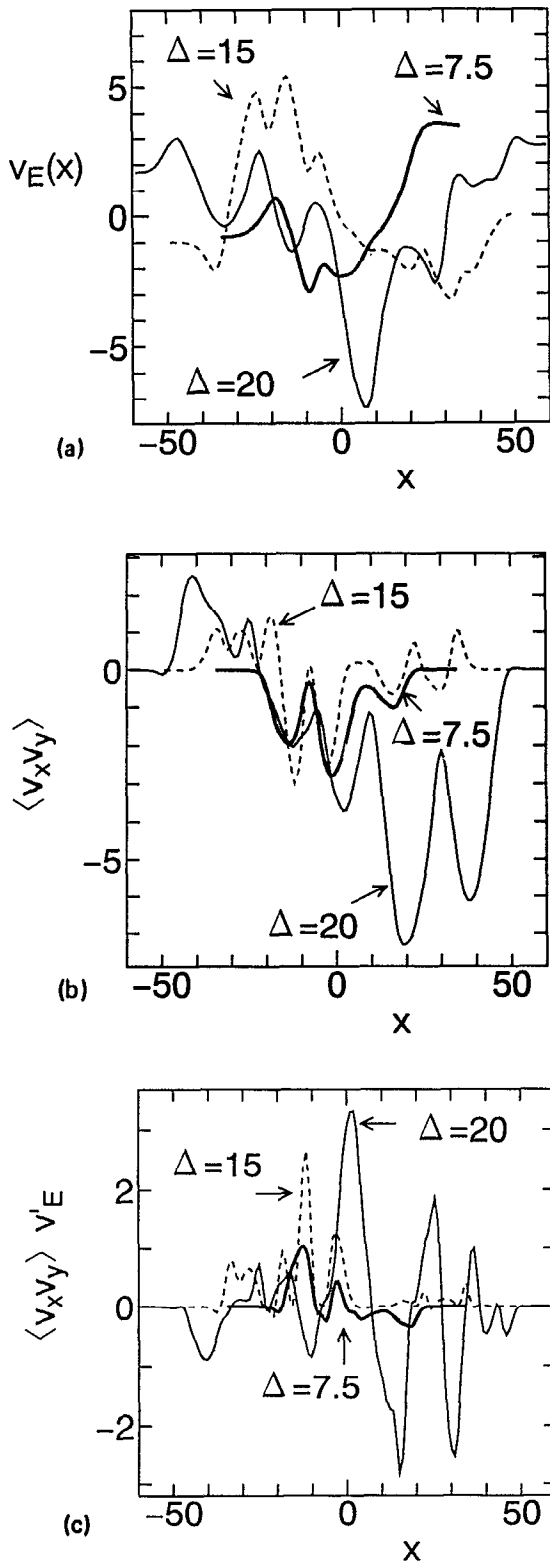
H. Sugama and W. Horton

FIG. 10. Radial profiles of (a) $v_E(x)$, (b) $\langle \tilde{v}_x \tilde{v}_y \rangle$, and (c) $\langle \tilde{v}_x \tilde{v}_y \rangle v_E'$ in the cases of Fig. 8 for $t=1500$.

the case of $\Delta=15$, the amplitudes of the $m=1$ modes with $n=\pm 1$ increase and become comparable to those of the $m=1$ modes with $n=0,\pm 2$. We argue that this reappearance of the $n=\pm 1$ modes is because the background shear flow causes a narrower radial mode structure and less interactions of the

$m=1$ modes with different m's. Due to this fact, the reduction of the total turbulence level by the shear flow is not so clear for $\Delta=15$ in Fig. 8. It is found from Fig. 10 that, compared to the case with $\Delta=7.5$ and compared to the single-helicity case, the background flow profile for $\Delta=20$ has more radial oscillations and accordingly the radial profile of transfer rate $\langle \tilde{v}_x \tilde{v}_y v_E' \rangle$ of turbulent kinetic energy to the mean flow is oscillating around zero, which appears to explain the difficulty with the shear flow suppression of the turbulent transport in the case of $\Delta=20$.

The poloidal acceleration by the Reynolds stress has the form of the radial derivative of the turbulent momentum flux. Therefore, by considering its radial integral, we find that the macroscopic variation of the poloidal flow with a large average value can be produced by the Reynolds stress only when the difference between the Reynolds stress at the inner and outer boundaries is large. The simulation results are now understood by observing that the poloidal flows with macroscopic shear profiles, which effectively suppress the turbulent transport, are produced by the single-helicity-like vortices with large radial scale lengths rather than by radial arrays consisting of a large number of small vortices.

IV. CONCLUSIONS

Thus the principal conclusions from these multiple helicity simulations of the resistive-g turbulent transport that include the generation of the background shear flow are as follows.

(i) In the multihelicity case, the large vortices (or convective cells) with low poloidal mode numbers suppress other modes around them. Within the width of the $m=1$ modes, there exists only a single peak in the convective flux profile even when there are mode rational surfaces within the mode width. Thus when the interactions between modes with different helicities are large, the total transport is not simply proportional to the radial distribution density of the unstable modes, since the neighboring interactions have essentially eliminated some of these modes. In an example given with $\Delta/W=7.5/20$, every other mode has been eliminated by the multihelicity nonlinear interactions so that the thermal flux is about one half that obtained by multiplying by the density of states as given by the Beklemishev–Horton[5] model.

The transport is a function of the density of the rational surfaces in contrast to the equipartition description in which each mode would be diminished equally with increasing mode density. In the highest density of rational surfaces case the transport is approximately three times the equipartition level.

(ii) When the number of vortices localized around different mode rational surfaces is large, the Reynolds stress produces radially oscillating background flow profiles, and the associated profile of the energy transfer from the turbulent kinetic energy to the background shear flow also oscillates around zero. Then the transport suppression by the turbulence driven shear flow is weak.

(iii) The simulations show that for the multiple helicity system the shear flow generation and turbulence suppression by momentum transport from $\rho \langle \tilde{v}_x \tilde{v}_y \rangle$ is more effective

Phys. Plasmas, Vol. 1, No. 7, July 1994

H. Sugama and W. Horton   2227

when there exists strong nonlinear interactions so that a few low-order rational surfaces with large vortices dominate the turbulence as in the single-helicity case.

The 3-D-multihelicity enhancement of the thermal transport by a factor of approximately 3 is similar to the enhancement found in the ion-temperature gradient drift shear flow problem.[8,9]

ACKNOWLEDGMENTS

The authors thank M. Okamoto (NIFS) and F. Waelbroeck (IFS) for encouragement and critical remarks during the course of this work. The numerical simulations were performed on the computer at the Theory and Computer Simulation Center at NIFS.

[1]B. A. Carreras, L. Garcia, and P. H. Diamond, Phys. Fluids **30**, 1388 (1987).
[2]H. Sugama and M. Wakatani, J. Phys. Soc. Jpn. **57**, 2010 (1988).
[3]B. A. Carreras, V. E. Lynch, and L. Garcia, Phys. Fluids B **5**, 1795 (1993).
[4]H. Sugama and W. Horton, Phys. Plasmas **1**, 345 (1994).
[5]A. Beklemishev and W. Horton, Phys. Fluids B **4**, 200 (1992).
[6]W. Horton, Phys. Rep. **192**, 123 (1990).
[7]S. Hamaguchi and W. Horton, Phys. Fluids. B **2**, 1833 (1990).
[8]X. N. Su, P. N. Yushmanov, J. Q. Dong, and W. Horton, Phys. Plasmas **1**, 1905 (1994).
[9]W. Dorland (private communication, 1993).

H. Sugama and W. Horton